HHS Public Access

Validation of a CT-based motion model with in-situ fluoroscopy for lung surface deformation estimation

M. Ranjbar[1,*], **P. Sabouri**[2,3,*], **S. Mossahebi**[2], **A. Sawant**[2], **P. Mohindra**[2], **G. Lasio**[2], **L.D. Timmie Topoleski**[1]

[1]Department of Mechanical Engineering, University of Maryland, Baltimore County

[2]Department of Radiation Oncology, University of Maryland, School of Medicine

[3]Department of Radiation Oncology, Miami Cancer Institute

Abstract

Many surrogate-based motion models (SMMs), proposed to guide motion management in radiotherapy, are constructed by correlating motion of an external surrogate and internal anatomy during CT-simulation. Changes in this correlation define model break down. We validate a methodology that incorporates fluoroscopic images (FL) acquired during treatment for SMM construction and update. Under a prospective IRB, 4DCT scans, VisionRT surfaces, and orthogonal FLs were collected from five lung cancer patients. VisionRT surfaces and two FL time-series were acquired pre- and post-treatment. A simulated annealing optimization scheme was used to estimate optimal lung deformations by maximizing the mutual information between digitally reconstructed radiographs (DRRs) of the SMM-estimated 3D images and FLs. Our SMM used partial-least-regression and was trained using the optimal deformations and VisionRT surfaces from the first breathing-cycle. SMM performance was evaluated using the mutual information score between reference FLs and the corresponding SMM or phase-assigned 4DCT DRRs. The Hausdorff distance for contoured landmarks was used to evaluate target position estimation error. For four out of five patients, two principal components approximated lung surface deformations with submillimeter accuracy. Analysis of the mutual information score between more than 4,000 pairs of FL and DRR demonstrated that our model led to more similarity between the FL and DRR images compared to 4DCT and DRR images from a model based on an a priori correlation model. Our SMM consistently displayed lower mean and 95th percentile Hausdorff distances. For one patient, 95th percentile Hausdorff distance was reduced by 11mm. Patient-averaged reductions in mean and 95th percentile Hausdorff distances were 3.6mm and 7mm for right-lung, and 3.1mm and 4mm for left-lung targets. FL data were used to evaluate model performance and investigate the feasibility of model update. Despite variability in breathing, use of post-treatment FL preserved model fidelity and consistently outperformed 4DCT for position estimation.

*These authors have contributed equally.

Introduction

Thoracoabdominal tumors are different from other tumors because they move and deform as the patient breaths. Tumor motion management strategies play an important role in the planning and delivery steps of modern thoracoabdominal radiation therapy (RT). Since direct monitoring of internal motion and deformation is not possible on the majority of today's linear accelerators (LINACs), alternative methods for long-term monitoring are required to estimate the internal anatomy during treatment delivery. To date, significant efforts have been made to construct models that use an easily accessible external surrogate to estimate internal lung and tumor motion.(McClelland, Hawkes et al. 2013) These surrogates serve to provide signals of high temporal resolution that when combined with acquired images, are used to develop time-dependent surrogate-based motion models (SMMs). Generation of such surrogate-based motion models (SMMs) requires estimating of internal lung motion from 4D imaging protocols, along with its *a priori* observed correlation with respect to the simultaneously acquired external surrogate.(Low, Parikh et al. 2005, Zhang, Pevsner et al. 2007, Zhang, Xu et al. 2008, Li, Lewis et al. 2011, Hinkle, Szegedi et al. 2012, Steiner, Shieh et al. 2019) For each observation of the surrogate, utilization of the model permits the generation of a new volumetric estimate of the internal anatomy. However, because of the large variability in human respiration, as well as the limited duration and availability of 4D imaging data over the course of RT, the training dataset used by these models is severely limited in terms of capturing cycle-to-cycle variations. Therefore, SMMs may resort to extrapolation beyond their training data when deviations from the training datasets are encountered. Expanding the model training dataset reduces this need for extrapolation which could potentially lead to improvements in model performance in the presence of cycle-to-cycle variations. For example, by using 25–30 fast helical CT scans acquired over a 2-minute duration (the 5D model), the image quality and temporal resolution of the training dataset can be improved. (Liu, Zhang et al. 2015) However, changes in the correlation between internal and external motion can compromise SMM performance. For example, prior studies in CyberKnife patients showed that tumor position prediction error significantly increased over 10-minute blocks (~1.6mm up to 5mm), indicating changes between tumor and respiratory surrogate displacement, which suggests the need for model update. (Pepin, Wu et al. 2011) As a result, commonly encountered variations in the *a priori* correlation can compromise model accuracy and limit clinical applicability. Consequently, the clinical use and implementation of such models require the ability to update the a priori model correlation. In addition, the model must be validated relevant to the in-situ setting that accounts for commonly encountered intra- and inter-fractional changes in the breathing pattern.

Current SMMs can be classified as imaging-based, biomechanical-based, or a hybrid of the two, depending on the approach used to estimate internal anatomical motion. Imaging-based models utilize the *a priori* observed correlation between the measured surrogate and the internal motion estimated using deformable image registration techniques.(Zeng, Fessler et al. 2007, McClelland, Hughes et al. 2010, Hinkle, Szegedi et al. 2012, McClelland, Hawkes et al. 2013, Ranjbar, Sabouri et al. 2018, Ranjbar, Sabouri et al. 2019, Steiner, Shieh et al. 2019) The multidimensional nature of motion in the thoracoabdominal region results

from the presence and interaction of several conditions including the complex nature of the airflow dynamics, engagement of several muscles with various levels of involvement, the presence of lung-chest wall sliding motion, and the existence of cardiac and esophageal motions such as swallowing. These conditions can limit model performance by interfering with the ability to compute accurate deformation vector fields (DVFs) or by creating motion that is absent in the external surrogate and not correlated to respiration. To overcome these difficulties, several intensity-based deformable image registration methods utilize multiple masks to separate anatomical regions, and adopt modifications such as penalty functions on voxel displacements, or regularization of sliding motion during optimization steps.(Rietzel, Pan et al. 2005, McClelland, Blackall et al. 2006, Al-Mayah, Moseley et al. 2007, Wu, Rietzel et al. 2008, Kyriakou and McKenzie 2011, Vandemeulebroucke, Rit et al. 2011) These methods can produce accurate DVFs in regions with high image gradient such as the lung boundaries. However, accurate DVF estimation inside the lung is challenging because of the inherent lack of intensity variations. Use of different deformable registration algorithms can potentially lead to substantially different DVFs for the lung interior. For example, Fatyga et al. compared algorithms selected to represent three classes of deformable image registration algorithms. While all three algorithms accurately estimated lung total volume and lung interface deformations, voxel-by-voxel subtraction of deformable image registration maps of the lung interior resulted in errors of more than one centimeter. (Fatyga, Dogan et al. 2015) Another multi-institutional evaluation of eight DIR algorithms using images from a deformable lung phantom reported maximum errors ranging between 5.1 and 15.4 mm, with greatest discrepancies observed inside the lung at areas of uniform image intensity with motion discontinuity. (Kashani, Hub et al. 2008) This study also highlighted the sensitivity of registration accuracy to the implemented technique, parameter setting and user differences. Aside from the noted image registration difficulties, another limitation of imaging-based models is that they rely on the *a priori* observed external-internal correlation without any consideration for physiological and mechanical principles. Because of the complex motion of the lung, and variations in the correlation between external surrogate and internal motion, these models can exhibit lower predictive power inside the lung. (McClelland, Hawkes et al. 2013, Han, Hawkes et al. 2014, Han, Dong et al. 2017)

Biomechanical-based models use numerical methods such as finite element analysis (FEA) to estimate respiration-induced deformations. These models take advantage of underlying physiological principles by considering tissue properties, lung topology, and lung surface boundary geometry to offer a realistic and robust mechanism for estimating the internal motion of the lung. (Brock, Dawson et al. 2006, Al-Mayah, Moseley et al. 2007, Werner, Ehrhardt et al. 2009, Tehrani, Yang et al. 2015, Cazoulat, Owen et al. 2016, Seyfi, Santhanam et al. 2016) Accurate lung surface boundary geometry conditions capture the expansion and contraction of the lung-surface during respiration to form a critical component of biomechanical-based SMMs. Assumptions regarding the material properties, and more importantly, simplifying the forces involved in the breathing, pose limitations in realistic modeling of the lung motion during respiration. Some of the limitations of imaging- and biomechanical-based models can be mitigated by using hybrid techniques, that combine the two. These techniques obtain the lung surface boundary geometry conditions from registration of 4D imaging data, and estimate internal motion of interest by FEA using

the optimized tissue material properties. Applicability of hybrid models for real-time motion management or post-treatment motion analysis is restricted by the lack of accurate lung surface boundary geometry and material properties. To date, the majority of these models have been restricted to variations in the "average" breathing cycle derived from 4D imaging data but have not been attempted for capturing intra- and inter-cycle variations that are commonly encountered in thoracic tumors.

In a previous study, we described an imaging-based SMM constructed using the 4DCT simulation data, and evaluated model performance using fluoroscopic (FL) scans of a single patient that were spread out over three RT fractions.(Ranjbar, Sabouri et al. 2019) Our results highlighted the ever-changing nature of the internal-external correlation and emphasized the breakdown of the a priori correlation with the external surrogate. These changes can stem from the relative nature of the surrogate (a limitation of currently available surrogates), or change in physiologic conditions. Several earlier studies have noted that the correlation between the external surrogate and internal motion is susceptible to change. (Vedam, Kini et al. 2003, Mageras, Pevsner et al. 2004, Fayad, Pan et al. 2011, Ehrhardt and Lorenz 2013) In this work, we present and validate a methodology that uses the thoracoabdominal surfaces as surrogate to generate new estimates of lung surface geometry that could potentially be used for numerical modeling of lung motion. Our methodology departs from the above noted literature, including our previous work, because it is not based on the *a priori* surrogate-internal correlation observed at the time of the initial CT simulation. Our current model uses the simulation data only to derive a mathematical representation of possible lung surface deformations and is constructed using the correlation observed during treatment delivery session, as constructed from FL imaging. Post-treatment FL data was used to evaluate the feasibility of exploiting additional FL imaging for model update. We present a qualitative and quantitative validation of our methodology and report our model accuracy under an in-situ setting during RT delivery sessions.

Methods

We propose an SMM that generates new estimates for lung surface boundary geometry by monitoring the thoracoabdominal surface via photogrammetry. The methodology for our proposed SMM is outlined in Figure 1 and is demonstrated using data collected from five lung cancer stereotactic body radiotherapy (SBRT) patients. The data processing and analysis consisted of three main procedures: (i) generation of the lung boundary surface deformations observed in 4DCT images, (ii) derivation of the relationship between a FL image and the lung surface deformation that resulted in that FL image, and (iii) generation of a model that related the external thoracoabdominal surface with the corresponding lung surface deformations. Subsequently, we validated our model by comparing the estimated motion of anatomical landmarks with their motion observed in FL projections that were used as "reference". The details associated with each procedure are described in the following sections.

Patient Data Collection

Data from five lung cancer stereotactic body radiation therapy (SBRT) patients (four males, one female with average age of 75) was acquired under IRB approval. These data consisted of 4DCT images, FL projections, and simultaneous photogrammetry surfaces obtained at the time of initial patient simulation and treatment sessions.

In our model construction, we used 10 phase-binned 4DCT images acquired on a Philips 16-slice Brilliance Big Bore scanner. The 4DCT scan lasted about 80 seconds and contained between 100–120 3-mm thick axial slices reconstructed on a 512×512 matrix, with pixel sizes ranging between 0.8 to 1.1 mm. The field of view was selected to capture the lung interface in all phases of the 4DCT. Concurrent with the 4DCT, VisionRT (VRT) surface data was acquired at ~15 Hz using a prototype, portable, couch mounted, VRT system. The prototype VRT unit consists of a speckle pattern projector and two cameras that are mounted on a portable frame. Figure 2-A shows the patient setup prior to the 4DCT and VRT surface data acquisition.

Prior to patient placement on the couch, the VRT system underwent standard calibration procedures. Following patient setup, the VRT system was placed over the patient's thighs, at approximately 80 cm from the xiphoid process. Further adjustments of the speckle pattern were performed according to the room lighting conditions, patient skin tone, and surface distance with respect to the camera.

FL projections and VRT surfaces were also acquired during treatment sessions and used for model construction, update, and validation. For each session, the collected data consisted of two sets of ~30 to 50 seconds-long FL projections with concurrently acquired VRT surfaces. After patient setup with cone beam-CT (CBCT), FL projections were acquired using the on-board kV imager (OBI) of the TrueBeam LINAC at the rate of 7 fps. For each scan, kVp was selected based on the patient's size with a source potential of 100–120kVp used for lateral projections (source at 270°) and a source potential of 80–100 kVp used for posterior-anterior (PA) projections (source at 180°). The FL and VRT data were acquired immediately prior to the start of the first treatment beam (start), and immediately following the last treatment beam (end). "Blade tracking", an option on the machine to reduce imaging dose, was used to collimate the kV source in congruence with the kV imager. The kV imager position was selected to best enable visualization of diaphragm motion. Table 1 reports the total number of continuous FL images and their duration used in this work.

Generation of Lung Surface Mesh and Deformable Image Registration

4DCT scans were imported into the RayStation (RS) Treatment Planning System (TPS, RaySearch Laboratories, Sweden), and the lung volume was manually contoured in all ten phases of the 4DCT. For image registration, the anatomically constrained deformation algorithm (ANACONDA) available in RS was used to deform the EE image (reference phase) into the remaining nine phases. (Weistrand and Svensson 2015, Kadoya, Nakajima et al. 2016) The deformations of the EE lung surface to other 4DCT phases were stored as lung surface-DVFs (SDVFs). The contoured lung surface was exported as a mesh of triangular elements containing nodes and connectivity (faces). Additionally, lung SDVFs,

the deformed EE lung mesh, and manual contours of the lung for each phase, body and the vertebral bodies mesh were stored for subsequent analysis. For numerical accuracy, a fine mesh representation of the lung surfaces was used. Total number of vertices in the EE lung surface mesh, and the EI and EE lung volumes are reported in Table 1. The mesh extraction process and examples of the acquired meshes are shown in the top row of Figure 3.

SDVF Dimensionality Reduction

Lung SDVFs for the N vertices belonging to the EE lung mesh (Table 1) were stored in a motion matrix $S = (S_j) \in \mathbb{R}^{9 \times (3 \times N)}$ with j denoting the rows of the motion matrix. Each row consisted of a lung SDVF from EE to the other 4DCT phases. Matrix S has $3 \times N$ columns which describe the 3D motion of each node. Since a fine triangular mesh was used to represent the lung surface, the motion matrix, S, contained approximately 360,000 entries. Principal component (PC) decomposition was used as a dimensionality reduction technique and each row of S was represented as a weighted sum of the mean deformation $\bar{S}_{mean}$ and the first n PC vectors, such that (Candès, Li et al. 2011, Hauberg, Feragen et al. 2014):

$$\widetilde{\mathbf{S}}^n_{50\% \to j} = \overline{\mathbf{S}}_{mean} + \sum_{i=1}^{n} \alpha^i_{50\% \to j} \mathbf{U_i} \quad \text{for } j \in \{0\%, 10\%, \ldots, 40\%, 60\%, \ldots, 90\%\} \tag{1}$$

where 0% and 50% denote the EI and EE phases respectively, $\mathbf{U_i}$ is the ith PC vector, the scalar $\alpha^i_{50\% \to j}$ represents the ith PC coefficient, and $\widetilde{\mathbf{S}}^n_{50\% \to j}$ is the approximated j^{th} row of S when the first n PCs were used in the summation.

The PC vectors $\mathbf{U_i}$ form an orthonormal set that represents the data stored in the motion matrix $\mathbf{S}$. For each vector $\mathbf{U_i}$, the set of vertices with non-zero entries correspond to regions whose motion is correlated along the direction $\mathbf{U_i}$. Because of the orthonormal condition of the PC vectors, the magnitude of the coefficients $\alpha^i_{50\% \to j}$ depends on the number of non-zero entries in $\mathbf{U_i}$ which in turn depends on the discretization of the lung surface. A larger magnitude $\alpha^i_{50\% \to j}$ is required to describe motion in densely populated vectors $\mathbf{U_i}$ such as the 1st or 2nd components. To avoid scaling artefacts in model generation, these coefficients were normalized to have zero mean and unit variance (calculated with respect to the 4DCT data-set) prior to their use.

Equation (1) provided a mechanism for reducing the dimensions of the dependent variables (lung SDVF) from three-times the number of mesh nodes to the n PC coefficients scalars a_j. For reasons explained in the results section, the first two PC coefficients ($i = 1,2$) were stored in the coefficient matrix $\mathbf{Y} = (\alpha^1_j, \alpha^2_j)$ and used for the subsequent analysis.

The 99th percentile absolute SDVF error (in mm) was used to examine the convergence rate of the PC approximation given by equation (1). The SDVF absolute error for the deformation from EE to phase j using the first n components was computed as:

$$\epsilon^n_j = \left| \widetilde{\mathbf{S}}^n_{50\% \to j} - \mathbf{S_j} \right| \tag{2}$$

where | | represents the Euclidean distance.

Reconstruction and Dimensionality Reduction of VRT Surfaces

Surface Reconstruction and Feature Extraction—The portable couch mounted VRT camera (AlignRT Inc, UK), shown in Figure 2, captured the thoracoabdominal surface at ~15 Hz during the initial CT simulation and RT delivery sessions. The benefit of using this system was that the same field of view was always maintained despite motion of the couch (e.g. during the CT-simulation). However, in comparison to clinical VRT systems, which typically have 2–3 units mounted on the ceiling, the single unit couch mounted system sat at a lower height over the patient's body and was more susceptible to geometric distortions. Examples of missing patches resulting from geometric and lighting distortions are shown in the VRT surface presented in Figure 4-A. To recover the missing data, we used the Poisson surface reconstruction algorithm to generate a water-tight surface on a 0.5×0.5 mm^2 grid (Figure 4-B). Previous phantom studies performed by our group have found this technique to have a 1 mm accuracy for tracking targets on the surface. (Ranjbar, Sabouri et al. 2019)

A region of interest (ROI) with a dimension of ~28×13 cm^2 that covered parts of thorax and abdomen was extracted from the VRT surfaces and used in all subsequent analysis. This region was selected to yield a signal-to-noise ratio (calculated using a cut-off frequency of 1/30 bpm) greater than 5% (100:5). Based on previous phantom studies by our group, this region typically lies about 2 cm interior of the point-cloud boundary. (Malinowski, McAvoy et al. 2012, Ranjbar, Sabouri et al. 2019)To further isolate and suppress the noise, compress the data, and interpolate the surface data into the FL time domain, we took advantage of isometric feature mapping (Isomap) as a dimensionality reduction technique.(Tenenbaum, De Silva et al. 2000) Using Isomap, three VRT surface features and the velocity of the first feature $\overrightarrow{\beta}(t) = \left(\beta^1(t), \beta^2(t), \beta^3(t), \dot{\beta}_1(t) \right)$ were extracted and used as model input. Figure 4-D presents the variations of the first surface feature $\beta_1(t)$ with the second and third features $\beta_2(t)$ and $\beta_3(t)$. The elongated elliptical path traced by the first surface feature and its derivative, $\dot{\beta}_1(t)$, is shown in Figure 4-E.

Synchronizing Surface and Fluoroscopic Measurements—To temporally synchronize the captured VRT surfaces and FL projections, we used intensity-based segmentation to approximate the motion of a patch on the diaphragm in the SI direction. Following data standardization, the motion of this patch was synchronized with the mean VRT ROI AP displacement. A camera frequency of 14.7 Hz with FL frequency of 7 Hz led to the best overlap between the two signals. This camera frequency was previously derived from phantom measurements.(Ranjbar, Sabouri et al. 2019) Two examples of the overlap for Patient 1 and 5 are shown in Figure 4-E and 4-F. For all patients, internal diaphragm patch motion, and external VRT signals overlapped well. Some differences between the two signals were particularly visible at the EI. Simulation and treatment setup for Patient 5 included an abdominal compression belt and larger deviations between the two signals were observed at the EE. By synchronizing the data temporally, we were able to associate each FL image with its corresponding surface features.

Model Construction and Validation

Associating Fluoroscopic Images with Lung SDVFs—We used FL images to derive a correspondence model between the external surrogate (VRT surfaces), and lung SDVF PC coefficients $\vec{\alpha}$. To do this, we assumed that the optimal PC coefficients, $\vec{\alpha}_{opt} = \left(\alpha_1^{opt}, \alpha_2^{opt}\right)$, results in a deformed lung surface whose projection, computed as a digitally reconstructed radiograph, most closely matches the corresponding FL frame. For each estimate of $\vec{\alpha}$, the corresponding EE lung surface was deformed using the SDVF approximated by equation (1). This deformed mesh was subsequently rasterized into a volumetric image with a 1 mm^3 resolution and assigned a density of 0.25 g/cm^3.(Pantaleoni 2011) In addition, the EE body and the vertebrae contours were rasterized onto the same image and assigned densities of 1.0 and 1.4 g/cm^3. Subsequently, a raytracing algorithm was used to reconstruct a radiographic projection of this volumetric image.(van Aarle, Palenstijn et al. 2015) Using the image mutual information score as the objective function, a simulated annealing optimization routine was used to arrive at the $\vec{\alpha}_{opt}$ that maximized the mutual information between the deformed lung radiograph, and the FL frame.(Xiang, Gubian et al. 2013) A search grid spanning four times the α_1 and α_2 magnitude that was observed at the time of the 4DCT was used to search for the optimal PC coefficients. Convergence was typically rapid and was reached within 100 iterations.

Correspondence Model between Surface Features and Lung SDVF Components

We used the extracted surface features, and optimized PC coefficients $\vec{\alpha}_{opt}(t)$ belonging to FL images in the first complete respiratory cycle (training set) to train a partial least square regression (PLSR) correspondence model. PLSR is a multivariate technique that has been applied in situations where few observations are available, and in a variety of fields such as medicinal chemistry, process control, and tumor classification to arrive at the relation between predictor and predicted variables. (Cramer, Patterson et al. 1988)

Using PLSR, the training data-set $\mathbf{Y} = \left(\vec{\alpha}_n(t)\right)$, and the corresponding surface feature components matrix, $\mathbf{X} = \left(\vec{\beta}_n(t)\right)$ were approximated as (Abdi and Williams 2013):

$$\mathbf{X} \sim \mathbf{T}\mathbf{P}^{\mathbf{T}} \tag{4}$$

$$\mathbf{Y} \sim \mathbf{T}\mathbf{B}\mathbf{C}^{\mathbf{T}} \tag{5}$$

where $\mathbf{T}$ is an orthonormal matrix referred to as the score matrix, $\mathbf{P}$ is the loading matrix with orthogonal columns, $\mathbf{C}$ is a weight matrix of dependent variables, and $\mathbf{B}$ is a diagonal matrix of regression weights. Utilizing the orthonormal property of the score matrix $\mathbf{T}$, and equations (4) and (5), the relation matrix $\mathbf{B}_{PLS} = (\mathbf{P}^{T})^{-1}\mathbf{B}\mathbf{C}^{T}$ was used to generate new estimates of the lung SDVF PC coefficient vector $\vec{y}(t) = \vec{\alpha}(t)$ for each new observation of surface features $\vec{x} = \vec{\beta}(t)$.

Model Validation and Performance

We manually tracked visible anatomical landmarks in FL images (assumed reference) and compared their positions with those visible in reconstructed radiographs of 3D lung surfaces generated by: 1) the model presented in this work, and 2) the corresponding 4DCT phase. For each FL frame in the validation data-set, its temporally corresponding surface features were input to the model and a new deformed lung mesh was estimated. Subsequently, the deformed lung mesh was rasterized and converted into a volumetric image, and a model estimated radiograph was reconstructed. Lung interface landmarks visible in each of these projections were contoured using the 3D-Slicer Software and their overlap was quantified using the 99th percentile Hausdorff distance metric (in mm).(Fedorov, Beichel et al. 2012, Taha and Hanbury 2015) This process was performed for the pair of FL time series that were acquired during one of the patient's treatment delivery session.

Qualitative model performance was evaluated by comparing the image mutual-information scores between the reference FL image and digitally reconstructed radiographs generated from three possible methods to estimate lung surface motion: 1) the model presented in this work, 2) the corresponding 4DCT phase, and 3) the 4DCT+VRT model that was proposed in our previous work. (Ranjbar, Sabouri et al. 2019) This analysis was performed for the pairs of FL time-series acquired over nine treatment delivery sessions of five lung SBRT patients (see Table 1).

Results

Lung Surface Deformation Vector Fields

Figure 5-A presents the motion map for the two lung SDVF PCs derived from 4DCT of Patient 1. The motion map highlights the relative motion of the lung surface and identifies regions that move together. Black regions correspond to locations on the lung surface where the PC vector, U_i, value was zero. Bright regions correspond to areas on the lung surface with non-zero entries signifying greater motion (white represents the maximum normalized motion). The third component had non-zero entries in only a few localized regions on the lung periphery and the pericardial sac. Analysis of the motion map for all patients showed that the region of motion becomes more localized and lower in magnitude for higher components.

Variation of the first PC coefficient with different 4DCT breathing phases is shown in Figure 5-B. While the sign of the coefficients depends on the specific direction for which vectors U_i in equation (1) were defined, the general pattern observed in most patients was that PC1 reached its extrema at the EE and returned near its EI value at 90% phase. Presence of binning artifacts that were present in Patient 3 violated this pattern (Patient 3). Figure 5-C presents the nearly identical circular pattern that was observed in all patients and depicts the variation between PC1 and PC2 representative of the average breathing cycle.

Convergence of the 99th percentile absolute SDVF error (in mm) with the increasing number of PCs used in equation (1) is shown in Figure 5-D. For four out of five patients, the absolute error converged to submillimeter accuracy after two components and plateaued thereafter with a slow convergence to zero. Convergence for Patient 3 was slower and plateaued after

four PCs. Analysis of this patient's 4DCT showed presence of binning artifacts particularly in the intermediate phases. As seen in Figure 5-E, intermediate phases such as 40%, and 60% also exhibited slow convergence.

Associating Fluoroscopic Images with Lung SDVFs

An example of the optimal lung with respect to a reference FL frame is shown in Figures 5-A and B respectively. The mutual information score as function of the PC coefficients, and the optimal values of those coefficients are shown in 5C. The mutual information score had a higher sensitivity with respect to a_1 than a_2. Figure 5D shows in this example (Patient1) the effects of those coefficients: a_1 affected the posterior portion of the diaphragm interface and a_2 affected the anterior portion of the diaphragm interface.

The deformations associated with the coefficients at the periphery of the search grid resulted in non-physical lung surfaces and distorted digitally reconstructed radiographs. These digitally reconstructed radiographs had a low mutual information score suggesting that the search grid was bounded.

Correspondence Model between Surface Features and Lung SDVF Components a

Figures 7-A and B present a comparison of the first PC coefficient $a_1(t)$ estimated by the model with and without update, 4DCT and our previous 4DCT+VRT model for the pre- and post-treatment fluoroscopic acquisitions. Data used for model training is shown in the shaded region. During the pre-treatment FL acquisition, 4DCT and 4DCT+VRT models estimated a cycle amplitude that was approximately twice the model estimated values, with the largest differences consistently observed at the peaks and valleys in the graph (EI and EE phases). Large differences between each method are also observed for the second PC coefficient $a_2(t)$ shown in Figure 7-C and D. Pre-treatment and post-treatment models also estimated different a_1 and a_2 values (green and black curves in Figure 7-B and D) suggesting a change in model coefficient.

A comparison of the model and 4DCT digitally reconstructed radiographs with the pre-treatment FL frame at t=13s is shown in Figure 7-C. The differences between the 4DCT radiograph and the reference FL image (2nd column) highlight some of the difficulties associated with using 4DCT when cycle-to-cycle breathing variations are encountered. Differences in diaphragm position at EE suggest a shift in the base line, with shallower exhales observed in comparison to the time of simulation, which the model correctly accounted for.

Model Validation

Figure 8 A–E presents box plot distributions of the mutual information calculated between reference FL images collected from nine pairs of pre- and post-treatment acquisitions (start and end), and the digitally reconstructed radiographs calculated from the current model (with and without updates), 4DCT lung surfaces (in red), and our previous 4DCT+ VRT model (in yellow). The reported model mutual information scores (in green) were calculated using the model trained with the pre-treatment FL (without update). Mutual information scores for the model updated with the post-treatment data are shown for the post-treatment

FLs (in black). In all instances, use of the model led to higher minimum and median mutual information scores, and smaller standard deviations (p<0.001). As observed from Figure 8-A, B, C, and E, for several acquisitions there were notable improvements compared to 4DCT or 4DCT+VRT. The higher mutual information scores imply better match between model digitally reconstructed radiographs and FL over 4DCT and suggest that digitally reconstructed radiographs generated from the model-estimated lung surfaces are a closer match to the reference FL over 4DCT. The smaller standard deviations imply a better consistency of these improvements. Some instances such as FX1-end for patient 1 (Figure 8-A) required model updates to preserve model fidelity. The pre-treatment model under performed in comparison to 4DCT while model fidelity was preserved in all cases when model was updated. In some cases, such as FX2 in panel B, and FX1-end in panel E, use of the 4DCT+VRT model led to degraded performance over 4DCT.

Model and 4DCT Hausdorff distance box plot distributions for five patients (P1–5) are shown in Figure 9 A1–A5. The second column of the figure displays the contoured landmarks (T) in each image set. For all patients and contoured landmarks, with the exception of P2-T4, model had smaller mean and 95th percentile errors (ϵ_{mean} and ϵ_{95}). 4DCT and model errors for P2-T4 target were within 1 mm. For several landmarks, improvements in model mean error and 95th percentile errors surpassed 3 mm, which is the lung SBRT planned-target-volume expansion margin at our institute. Differences between model and 4DCT 95th percentile error, $_{95}$, were notable for the diaphragm-right lobe interface such as P1-T1 ($_{95}$ =9mm), P2-T3 ($_{95}$ =8 mm), P3-T3($_{95}$ = 9 mm) and P4-T2,T3 ($_{95}$ =8 and 5 mm). Improvement in mean and 95th percentile error for the right lobe diaphragm, averaged over all patients, were $_{mean}$ = 3.6 and $_{95}$ = 6.5 mm, respectively. In comparison, improvements in model performance for the diaphragm-left lobe interface were slightly reduced. Notable examples include P1-T2 ($_{95}$ =4.6mm), P3-T1 ($_{95}$ = 3.44 mm) and P4-T1 ($_{95}$ =11 mm). For the diaphragm-left lobe interface, difference between model and 4DCT Mean and 95th percentile errors for all patients were $_{mean}$ = 3.1 and $_{95}$ = 4.1 mm, respectively. The largest errors were observed for structures associated with the pericardial sac such as P4-T4 (ϵ_{mean}^{model} = 15 mm, $_{95}$ = 0.3 mm), and P5-T4 (ϵ_{mean}^{model} = 7 mm, $_{95}$ = 4.2).

Discussion

We presented a motion model that estimates lung surface DVFs by monitoring the motion of an ROI on the thoracoabdominal surface. Our proposed model employed a mathematical framework of the possible deformations derived from deformable image registration of 4DCT images and integrated additional FL images to derive and update the internal-external correlation. To date, 4DCT based volumetric motion models have been constructed based on the *a priori* correlation between the external surrogate and internal anatomy that was observed at the time of 4DCT simulation. (Zhang, Pevsner et al. 2007, Li, Lewis et al. 2011, Ranjbar, Sabouri et al. 2019) Our methodology departed from this approach and exploited FL images to relate the external surrogate to the internal motion of the lung surface and to derive an internal-external correlation that was more accurate and applicable during RT delivery sessions. Additionally, our methodology permitted for continuous model updates,

which preserved model fidelity in cases where inter- or intra-fraction changes in correlation were observed. Finally, we presented a model-agnostic, in-situ validation technique based on the comparison of the image mutual information and the motion of anatomical landmarks that were manually tracked in model-generated radiographic projections, 4DCT-radigraphic projections, and reference FL projections. Our results indicated a marked improvement over the current standard-of-care 4DCT with average reduction in 95th percentile Hausdorff distance of 7 mm for the left-lobe diaphragm interface, and 4 mm for the right lobe diaphragm interface.

In a previous study, we presented a preliminary investigation of a volumetric based SMM that used the external-internal correlation observed at the time of 4DCT to generate new estimates of the internal anatomy.(Ranjbar, Sabouri et al. 2019) The present study differs from that work in the utilized image registration algorithms, dimensionality reduction procedure for the imaging data, as well as the surrogate extraction and its dimensionality reduction technique. More significantly, the current study departs from our previous work, as well as most published volumetric motion models, in its training data-set. The training data-set forms the foundation of the motion model and is used to arrive at the correlation between the internal anatomy and the continuous external surrogate. The training data for our previous study was composed of VRT surfaces and 4DCT data acquired at the time of the initial CT simulation. However, as a byproduct of the axial 4DCT data acquisition and binning, the reconstructed 4DCT image set does not correspond to any physical anatomical state but rather phase-sorted and binned axial slices that represent discrete approximations of the patient's "average" anatomy during each breathing phase. As a result, it is difficult to relate these images with the concurrently acquired external VRT surrogate. In the previous study, we resorted to using a synthetic surface data-set that was generated by averaging all VRT surfaces belonging to a specific phase. In addition to the previously noted limitations that arise from the application of this *a priori* correlation to the upcoming RT sessions, a major drawback of this approach is the pairing of two incoherent measurements: an axially acquired phase-binned 4DCT image with a temporally averaged VRT surface. Such incoherence is accentuated in the cases of departure from periodic breathing such as the presence of cycle-to-cycle variations. One immediate example of such an incoherence is encountered when 4DCT images that suffer from commonly encountered binning artifacts are paired with temporally phase-averaged VRT surfaces. A consequence of such artifacts is the erroneous patterns for the evolution of the first PC coefficient as seen for Patient 3 in Figure 5-B. However, given the spatially instantaneous nature of the VRT surface, such a pattern was not present in the temporally phase-averaged VRT surfaces of this patient. The present study not only avoids this association altogether, but also derives and updates the internal external correlation at the time of the RT sessions. In our proposed methodology, 4DCT images are used solely to derive a mathematical basis of internal anatomical motions. Subsequently, the internal-external correlation is derived and updated using the continuous FL images with simultaneous VRT surfaces. With respect to respiratory motion, both of these measurements can be considered instantaneous such that their pairing into the training data-set is coherent. Qualitative analysis of model performance (Figure 8) showed that in comparison to our previous 4DCT+VRT model, the current strategy systematically generated projections that more closely matched the reference fluoroscopy

and yielded higher image mutual information scores observed for all patients. For the single patient studied in our previous work (Patient 1 of this study), the 4DCT+VRT model was affected by temporal changes in the external-internal correlation, and had inconsistent performance, with errors as large as 15 mm for diaphragm motion. The current motion model integrates a few FL images (equivalent to one respiratory cycle) to establish the external-internal correlation for ~30–50s FL acquisitions. Using the proposed methodology, the diaphragm motion error for this patient was reduced to 6 mm (Figure 9-A). This strategy was found to preserve model fidelity in the cohort of five patients presented in this study. We presented a model validation by comparing image similarity for nine pairs of FL acquisitions -approximately 10 minutes of data. The higher image similarity coefficients provided a qualitative assessment of the model performance while tracking the manually contoured anatomical landmarks provided a quantitative validation.

High image contrast facilitated DVF estimates at the lung boundary. Additionally, the strong correlation between the external surrogate and the motion of the lung-diaphragm interface has been reported in multiple studies.(Li, Xie et al. 2009, Fayad, Pan et al. 2011) Those characteristics provided us with the confidence to estimate deformations of the lung surface based on the thoracoabdominal surface. Moreover, the visible nature of the lung boundary in lateral and fluoroscopic images provided a framework to validate our estimated lung deformations. Previous applications of PCA to DVFs in RT, including our previous work, present a feasible way to provide an estimate for the deformations of the lung tumor.(Zhang, Pevsner et al. 2007, Li, Lewis et al. 2011, Garau, Via et al. 2019, Ranjbar, Sabouri et al. 2019) However, there are multiple factors that challenge the accuracy of model estimates of tumor/GTV motion. There is the complexity of lung interior motion, including deviations in tumor trajectory, temporal phase differences in the GTV motion, possible registration errors within the lung, and the inherently low contrast of fluoroscopic images in this anatomical region that strongly limit the visibility of targets. For these reasons, we have not applied the technique presented in this work to estimate DVFs of the entire volumetric image including the GTV-even though it would be possible to do so. Our group is currently pursuing finite-element modeling of internal lung motion that exploits the biomechanical properties of the lung and underlying physical and biomechanical principles to estimate motion in the lung-interior. To date, the high accuracy of such models reported for estimation of GTV motion within the same CT series provides a promising approach for application to treatment. The lung surface deformations presented in this work would serve as boundary condition input for such a model to estimate tumor motion during RT delivery.

This study employed dimensionality reduction at multiple stages to reduce the complexity of the model, synchronize different modalities of measurements, and increase computational speeds. Using isometric embedding (Isomap), we recovered three independent features from the thoracoabdominal surfaces captured by photogrammetry. These first feature signals were temporally correlated with the SI motion of a region on the diaphragm (Figure 4 F and G), which was temporally used to associate the external surrogate with each frame in the fluoroscopic time-series. While further investigation is required, the presence of these independent signals may be related to the fashion in which respiratory motion is physiologically actuated by independent muscle groups such as the major abdominal muscles including the diaphragm, as well as the intercostal muscles of the thorax.

Non-linear manifold learning techniques such as Isomap excel at finding a low dimensional embedding of the original data. However, the transformations associated with such methods are not invertible and there does not exist a reliable reconstruction from the low dimensional space back to the original high dimensional space. (Choi and Choi 2007) For this reason, in instances where recovery of the data after dimensionality reduction was required, we resorted to linear dimensionality reduction techniques such as PCA. In the field of mathematical lung motion models, PCA has been widely used for the reduction of DVF dimensions.(Zhang, Pevsner et al. 2007, Li, Lewis et al. 2011, Ranjbar, Sabouri et al. 2019) Our analysis of five patients showed that two components are generally adequate for approximation of lung SDVFs (Figure 5D). These findings are in agreement with reports of Zhang et al., and Li et al. who presented 90 convergence of volumetric DVFs for two thoracic patients.(Zhang, Pevsner et al. 2007, Li, Lewis et al. 2011)

One major limitation in this work is the use of single direction projection fluoroscopy in deriving appropriate model coefficients. It has been accepted in RT that the anatomy can be appropriately localized using two orthogonal radiographs. This principle is routinely applied during patient setup with kV orthogonal radiographs. Our study presented results for both posterior-anterior, and lateral projections. However, at each time instance, the single kV imager on the TrueBeam only permitted FL acquisition in a single direction, so that simultaneous orthogonal image acquisition was not possible. This limitation can be alleviated through the use of other commercially available imaging systems such as Exac Trac (BrainLAB, Germany), or the CyberKnife Synchrony (Accuray, CA), ProBeam (Varian, Germany).(Matney, Parker et al. 2011, Pepin, Wu et al. 2011) We believe that the use of two orthogonal radiographs will increase the sensitivity of the optimization function to higher order PC coefficients, and provide more accurate estimates for higher order coefficients.

Another limitation in this work stems from its use of phase-binned 4DCT images. While this protocol is the current standard-of-care in thoracic RT, previous studies have noted that more than 90% of such CT scans suffer from imaging artifacts.(Yamamoto, Langner et al. 2008) Use of principle component analysis has been shown to potentially reduce some of these artifacts.(Gao, Cai et al. 2011) Phase-sorting related errors can also generate artifact contaminated DVFs which hinder convergence with increasing PCs (e.g. Patient 3 in Figure 6-D). These errors are subsequently propagated into the motion model and manifest themselves as incorrect model-estimated deformations. Use of repeated fast helical CT protocols that integrate multiple scan samples of the same breathing cycle have been shown to remove 4DCT phase-binning artifacts and produce superior image quality in the presence of irregular breathing. Such scans can provide more accurate DVFs, as well a higher quality pivot phase image EE image and are expected to improve overall model accuracy. (Thomas, Lamb et al. 2014) Other techniques to reduce 4DCT image artifacts include integration of motion models in the CT reconstruction algorithm. Recently, Chee et al. proposed an imaging based SMM for CBCT reconstruction artifact reduction that used DVFs between reference and target frames of binned 4DCT images that were derived from the surrogate-estimated diaphragm displacement amplitude and its derivative. (Chee, O'Connell et al. 2019) While computationally expensive (requiring 200 hours for model construction), a virtual phantom study of their model using the XCAT phantom showed

high spatial accuracy DVF estimations with errors of 1.08±0.81 mm. While their model requires validation with patient data, their methodology has the potential to significantly reduce artifacts associated with 4DCT imaging protocols.

Higher image quality produces more accurate DVFs and improves overall model performance. However, the major drawback associated with the use of 4DCT is the lack of adequate observations, which hinders derivation of a robust mathematical basis of possible anatomical deformations. In our study, we generally observed degraded model performance for regions near the GI tract (e.g. left lung lobe-diaphragm interface). Short-term displacement of the lung interface in this region is primarily due to respiratory motion, with a correlated motion expected between the two lobes (e.g. Figure 6-A); however, filling and displacement of organs in the GI tract can result in the shift of a single lobe from the base-line observed at the time of 4DCT. Since such displacements are not present in the 4DCT scan session, they cannot be accounted for in the orthonormal DVF expansion from these images. With the advent of a more imagebased adaptive RT, routine QA-4DCT scans, and in-situ 4D-CBCTs are becoming a part of the standard-of-care in particle therapy or dose-escalated SBRT. Integration of additional imaging data can potentially generate more accurate DVF basis and improve overall model performance.

Another limitation of this work was the relatively short duration of FL data acquisition (~30–50 seconds) to limit the unnecessary exposure of the patient to radiation. One of the main goals of this study was to validate the model. Therefore, we maximized the data available for validation by using only one to two cycles for training. Using more cycles for training may improve the model performance and robustness but requires further investigation and additional data for validation. For example, longer and safer data acquisition maybe possible using non-radiological imaging modalities such as MRI.

Our model used kV fluoroscopic projections and a global optimization scheme to arrive at optimal DVFs. The wide availability of kV images in external beam radiation therapy makes their integration into a CT based motion model valuable. However, the compounding nature of kV images which are convoluted by the many layers of information that they possess makes their use a particularly difficult task. Recently, Garau et al. attempted to mitigate the effects of cycle-to-cycle variations by integrating in-vivo 2D cine MRI data acquired on an MR-LINAC system.(Garau, Via et al. 2019) Their model estimates time-resolved virtual 3D-CT volumes describing the patient anatomy during treatment. However, due to the registration strategy between breath-hold MR and 4DCT images, the model was unable to capture inter-fractional changes. While limited in its availability, integration of in-vivo MR data with the global optimization strategy presented in this work can potentially lead to realistic estimation of GTV motion in time resolved 3DCT images.

Our model generated estimates of the lung surface including the location of the diaphragm-lung interface at each lobe. The motions of these landmarks are commonly assessed and used as an internal surrogate prior to treatment delivery under breath-hold and free-breathing gated RT delivery. While requiring faster computational times, one possible application of our model is to permit visualization and verification of these landmarks during treatment delivery. Additionally, coupled with a biomechanical model of the lung interior, our model

has the potential to provide internal motion estimation for dose accumulation over the course of treatment delivery. Knowledge of the internal anatomical motion can reduce uncertainties in the process, and subsequently help identify uncertainties in delivery/planning. A hybrid biomechanical intensity-based model with the BCs generated using our methodology can aid in determining accurate deformations at the time of patient treatment delivery, and serve as a gold standard for the comparison and validation of imaging-based motion models.

Conclusion

We constructed and updated a volumetric motion model that used the correlation observed from in-situ fluoroscopic projections acquired at the time of treatment delivery. This model consistently out-performed 70 4DCT for position estimation of targets on the lung surface. Despite changes in the breathing pattern, including base-line shifts, routine update of the internal-external correlation preserved model fidelity. Our model provides input boundary conditions for hybrid and/or biomechanical-based lung motion models and also has the potential to improve delivery verification and accuracy by providing the motion of internal surrogates which are often used to assess tumor position during breath-hold and free-breathing gated radiation treatment delivery.

Acknowledgements

References

Abdi H and Williams LJ (2013). Partial least squares methods: partial least squares correlation and partial least square regression. Computational toxicology, Springer: 549–579.

Al-Mayah A, Moseley J and Brock K (2007). "Contact surface and material nonlinearity modeling of human lungs." Physics in Medicine & Biology 53(1): 305. [PubMed: 18182705]

Brock KK, Dawson LA, Sharpe MB, Moseley DJ and Jaffray DA (2006). "Feasibility of a novel deformable image registration technique to facilitate classification, targeting, and monitoring of tumor and normal tissue." International Journal of Radiation Oncology* Biology* Physics 64(4): 1245–1254.

Candès EJ, Li X, Ma Y and Wright J (2011). "Robust principal component analysis?" Journal of the ACM (JACM) 58(3): 11.

Cazoulat G, Owen D, Matuszak MM, Balter JM and Brock KK (2016). "Biomechanical deformable image registration of longitudinal lung CT images using vessel information." Physics in Medicine & Biology 61(13): 4826. [PubMed: 27273115]

Chee G, O'Connell D, Yang Y, Singhrao K, Low D and Lewis J (2019). "McSART: an iterative modelbased, motion-compensated SART algorithm for CBCT reconstruction." Physics in Medicine & Biology 64(9): 095013. [PubMed: 30776788]

Choi H and Choi S (2007). "Robust kernel isomap." Pattern Recognition 40(3): 853–862.

Cramer RD, Patterson DE and Bunce JD (1988). "Comparative molecular field analysis (CoMFA). 1. Effect of shape on binding of steroids to carrier proteins." Journal of the American Chemical Society 110(18): 5959–5967. [PubMed: 22148765]

Ehrhardt J and Lorenz C (2013). 4D modeling and estimation of respiratory motion for radiation therapy, Springer.

Fatyga M, Dogan N, Weiss E, Sleeman IV WC, Zhang B, Lehman WJ, Williamson JF, Wijesooriya K and Christensen GE (2015). "A voxel-by-voxel comparison of deformable vector fields obtained by three deformable image registration algorithms applied to 4DCT lung studies." Frontiers in Oncology 5: 17. [PubMed: 25699238]

Fayad H, Pan T, François Clement J and Visvikis D (2011). "Correlation of respiratory motion between external patient surface and internal anatomical landmarks." Medical physics 38(6Part1): 3157–3164. [PubMed: 21815390]

Fedorov A, Beichel R, Kalpathy-Cramer J, Finet J, Fillion-Robin J-C, Pujol S, Bauer C, Jennings D, Fennessy F and Sonka M (2012). "3D Slicer as an image computing platform for the Quantitative Imaging Network." Magnetic resonance imaging 30(9): 1323–1341. [PubMed: 22770690]

Gao H, Cai J-F, Shen Z and Zhao H (2011). "Robust principal component analysis-based four-dimensional computed tomography." Physics in Medicine & Biology 56(11): 3181. [PubMed: 21540490]

Garau N, Via R, Meschini G, Lee D, Keall PJ, Riboldi M, Baroni G and Paganelli C (2019). "A ROI-based global motion model established on 4DCT and 2D cine-MRI data for MRI-guidance in radiation therapy." Physics in medicine and biology.

Han L, Dong H, McClelland JR, Han L, Hawkes DJ and Barratt DC (2017). "A hybrid patient-specific biomechanical model based image registration method for the motion estimation of lungs." Medical image analysis 39: 87–100. [PubMed: 28458088]

Han L, Hawkes D and Barratt D (2014). A hybrid biomechanical model-based image registration method for sliding objects. Medical Imaging 2014: Image Processing, International Society for Optics and Photonics.

Hauberg S, Feragen A and Black MJ (2014). Grassmann averages for scalable robust PCA. Proceedings of the IEEE Conference on Computer Vision and Pattern Recognition.

Hinkle J, Szegedi M, Wang B, Salter B and Joshi S (2012). "4D CT image reconstruction with diffeomorphic motion model." Medical image analysis 16(6): 1307–1316. [PubMed: 22766457]

Kadoya N, Nakajima Y, Saito M, Miyabe Y, Kurooka M, Kito S, Fujita Y, Sasaki M, Arai K and Tani K (2016). "Multi-institutional validation study of commercially available deformable image registration software for thoracic images." International Journal of Radiation Oncology* Biology* Physics 96(2): 422–431.

Kashani R, Hub M, Balter JM, Kessler ML, Dong L, Zhang L, Xing L, Xie Y, Hawkes D and Schnabel JA (2008). "Objective assessment of deformable image registration in radiotherapy: a multi-institution study." Medical physics 35(12): 5944–5953. [PubMed: 19175149]

Kyriakou E and McKenzie D (2011). "Dynamic modeling of lung tumor motion during respiration." Physics in Medicine & Biology 56(10): 2999. [PubMed: 21508446]

Li G, Xie H, Ning H, Lu W, Low D, Citrin D, Kaushal A, Zach L, Camphausen K and Miller RW (2009). "A novel analytical approach to the prediction of respiratory diaphragm motion based on external torso volume change." Physics in Medicine & Biology 54(13): 4113. [PubMed: 19521009]

Li R, Lewis JH, Jia X, Zhao T, Liu W, Wuenschel S, Lamb J, Yang D, Low DA and Jiang SB (2011). "On a PCA-based lung motion model." Physics in Medicine & Biology 56(18): 6009. [PubMed: 21865624]

Liu J, Zhang X, Zhang X, Zhao H, Gao Y, Thomas D, Low DA and Gao H (2015). "5D respiratory motion model based image reconstruction algorithm for 4D cone-beam computed tomography." Inverse Problems 31(11): 115007.

Low DA, Parikh PJ, Lu W, Dempsey JF, Wahab SH, Hubenschmidt JP, Nystrom MM, Handoko M and Bradley JD (2005). "Novel breathing motion model for radiotherapy." International Journal of Radiation Oncology* Biology* Physics 63(3): 921–929.

Mageras GS, Pevsner A, Yorke ED, Rosenzweig KE, Ford EC, Hertanto A, Larson SM, Lovelock DM, Erdi YE and Nehmeh SA (2004). "Measurement of lung tumor motion using respirationcorrelated CT." International Journal of Radiation Oncology* Biology* Physics 60(3): 933–941.

Malinowski K, McAvoy TJ, George R, Dietrich S and D'Souza WD (2012). "Incidence of changes in respiration-induced tumor motion and its relationship with respiratory surrogates during individual treatment fractions." International Journal of Radiation Oncology* Biology* Physics 82(5): 1665–1673.

Matney JE, Parker BC, Neck DW, Henkelmann G and Rosen II (2011). "Target localization accuracy in a respiratory phantom using BrainLab ExacTrac and 4DCT imaging." Journal of applied clinical medical physics 12(2): 301–309.

McClelland JR, Blackall JM, Tarte S, Chandler AC, Hughes S, Ahmad S, Landau DB and Hawkes DJ (2006). "A continuous 4D motion model from multiple respiratory cycles for use in lung radiotherapy." Medical Physics 33(9): 3348–3358. [PubMed: 17022231]

McClelland JR, Hawkes DJ, Schaeffter T and King AP (2013). "Respiratory motion models: a review." Medical image analysis 17(1): 19–42. [PubMed: 23123330]

McClelland JR, Hughes S, Modat M, Qureshi A, Ahmad S, Landau D, Ourselin S and Hawkes D (2010). "Inter-fraction variations in respiratory motion models." Physics in Medicine & Biology 56(1): 251. [PubMed: 21149951]

Pantaleoni J (2011). VoxelPipe: A programmable pipeline for 3D voxelization. Proceedings of the ACM SIGGRAPH Symposium on High Performance Graphics.

Pepin EW, Wu H, Zhang Y and Lord B (2011). "Correlation and prediction uncertainties in the cyberknife synchrony respiratory tracking system." Medical physics 38(7): 4036–4044. [PubMed: 21859002]

Ranjbar M, Sabouri P, Mossahebi S, Leiser D, Foote M, Zhang J, Lasio G, Joshi S and Sawant A (2019). "Development and prospective in-patient proof-of-concept of a surface photogrammetry+ CT-based volumetric motion model for lung radiotherapy." Medical physics.

Ranjbar M, Sabouri P, Mossahebi S, Leiser D, Foote M, Zhang J, Lasio G, Joshi S and Sawant A (2019). "Development and prospective in-patient proof-of-concept validation of a surface photogrammetry+ CT-based volumetric motion model for lung radiotherapy." Medical physics 46(12): 5407–5420. [PubMed: 31518437]

Ranjbar M, Sabouri P, Repetto C and Sawant A (2018). An Externally and Internally Deformable Lung Motion Phantom with Programmable, Variable External-Internal Correlation. MEDICAL PHYSICS, WILEY 111 RIVER ST, HOBOKEN 07030–5774, NJ USA.

Ranjbar M, Sabouri P, Repetto C and Sawant A (2019). "A novel deformable lung phantom with programably variable external and internal correlation." Medical physics 46(5): 1995–2005. [PubMed: 30919974]

Rietzel E, Pan T and Chen GT (2005). "Four-dimensional computed tomography: image formation and clinical protocol." Medical physics 32(4): 874–889. [PubMed: 15895570]

Seyfi B, Santhanam AP and Ilegbusi OJ (2016). "A biomechanical model of human lung deformation utilizing patient-specific elastic property." Journal of Cancer Therapy 7(06): 402.

Steiner E, Shieh C-C, Caillet V, Booth J, O'Brien R, Briggs A, Hardcastle N, Jayamanne D, Szymura K, Eade T and Keall P (2019). "Both four-dimensional computed tomography and four-dimensional cone beam computed tomography under-predict lung target motion during radiotherapy." Radiotherapy and Oncology 135: 65–73. [PubMed: 31015172]

Taha AA and Hanbury A (2015). "An efficient algorithm for calculating the exact Hausdorff distance." IEEE transactions on pattern analysis and machine intelligence 37(11): 2153–2163. [PubMed: 26440258]

Tehrani JN, Yang Y, Werner R, Lu W, Low D, Guo X and Wang J (2015). "Sensitivity of tumor motion simulation accuracy to lung biomechanical modeling approaches and parameters." Physics in Medicine & Biology 60(22): 8833. [PubMed: 26531324]

Tenenbaum JB, De Silva V and Langford JC (2000). "A global geometric framework for nonlinear dimensionality reduction." science 290(5500): 2319–2323. [PubMed: 11125149]

Thomas D, Lamb J, White B, Jani S, Gaudio S, Lee P, Ruan D, McNitt-Gray M and Low D (2014). "A novel fast helical 4D-CT acquisition technique to generate low-noise sorting artifact–free images at user-selected breathing phases." International Journal of Radiation Oncology* Biology* Physics 89(1): 191–198.

van Aarle W, Palenstijn WJ, De Beenhouwer J, Altantzis T, Bals S, Batenburg KJ and Sijbers J (2015). "The ASTRA Toolbox: A platform for advanced algorithm development in electron tomography." Ultramicroscopy 157: 35–47. [PubMed: 26057688]

Vandemeulebroucke J, Rit S, Kybic J, Clarysse P and Sarrut D (2011). "Spatiotemporal motion estimation for respiratory-correlated imaging of the lungs." Medical physics 38(1): 166–178. [PubMed: 21361185]

Vedam S, Kini V, Keall P, Ramakrishnan V, Mostafavi H and Mohan R (2003). "Quantifying the predictability of diaphragm motion during respiration with a noninvasive external marker." Medical physics 30(4): 505–513. [PubMed: 12722802]

Weistrand O and Svensson S (2015). "The ANACONDA algorithm for deformable image registration in radiotherapy." Medical physics 42(1): 40–53. [PubMed: 25563246]

Werner R, Ehrhardt J, Schmidt R and Handels H (2009). "Patient-specific finite element modeling of respiratory lung motion using 4D CT image data." Medical physics 36(5): 1500–1511. [PubMed: 19544766]

Wu Z, Rietzel E, Boldea V, Sarrut D and Sharp GC (2008). "Evaluation of deformable registration of patient lung 4DCT with subanatomical region segmentations." Medical physics 35(2): 775–781. [PubMed: 18383700]

Xiang Y, Gubian S, Suomela B and Hoeng J (2013). "Generalized Simulated Annealing for Global Optimization: The GenSA Package." R Journal 5(1).

Yamamoto T, Langner U, Loo BW Jr, Shen J and Keall PJ (2008). "Retrospective analysis of artifacts in four-dimensional CT images of 50 abdominal and thoracic radiotherapy patients." International Journal of Radiation Oncology* Biology* Physics 72(4): 1250–1258.

Zeng R, Fessler JA and Balter JM (2007). "Estimating 3-D respiratory motion from orbiting views by tomographic image registration." IEEE Transactions on Medical Imaging 26(2): 153–163. [PubMed: 17304730]

Zhang J, Xu XG, Shi C and Fuss M (2008). "Development of a geometry-based respiratory motion–simulating patient model for radiation treatment dosimetry." Journal of Applied clinical medical physics 9(1): 16–28. [PubMed: 18716584]

Zhang Q, Pevsner A, Hertanto A, Hu YC, Rosenzweig KE, Ling CC and Mageras GS (2007). "A patient-specific respiratory model of anatomical motion for radiation treatment planning." Medical physics 34(12): 4772–4781. [PubMed: 18196805]
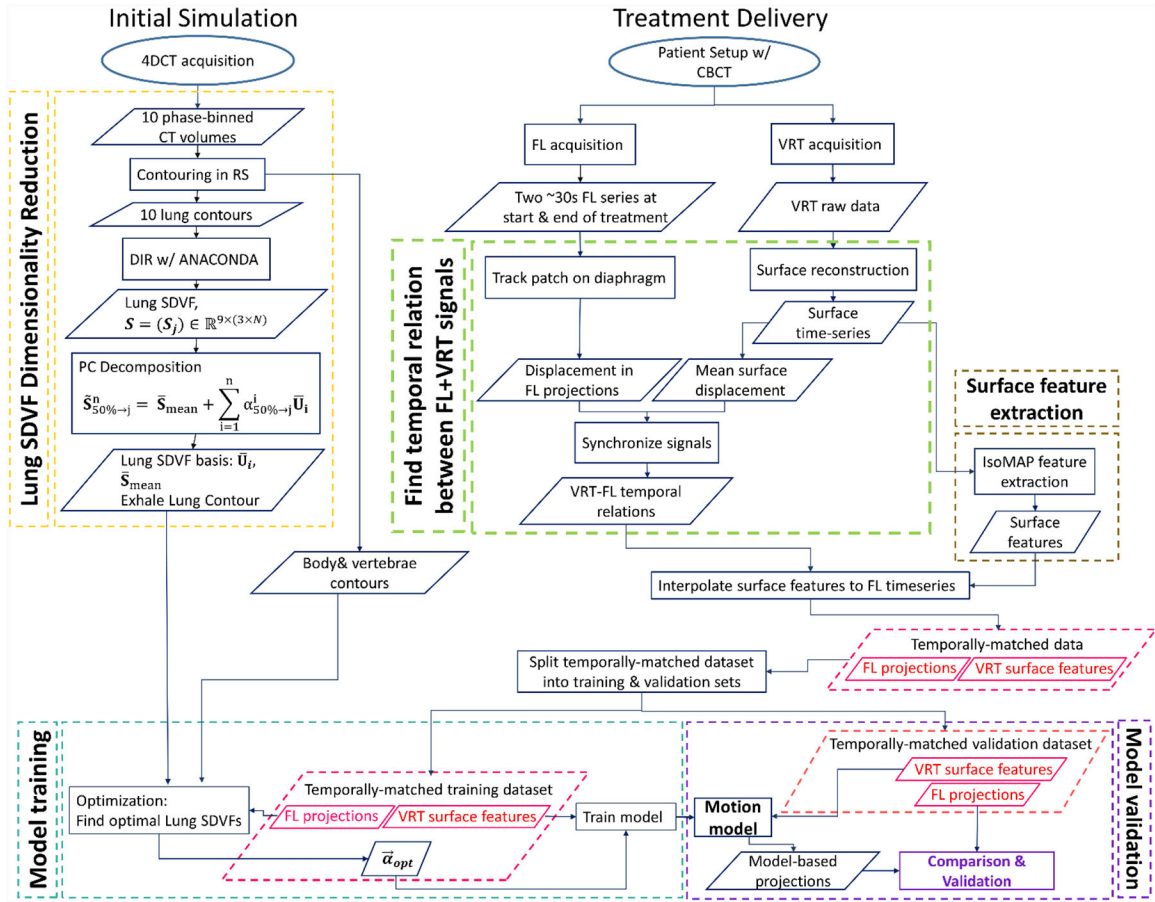
Figure 1- Flowchart of the methodology used to construct and validate our proposed motion model:

Deformable image registration (DIR) was used in the RayStation Treatment Planning System and principal component analysis (PCA) was applied to arrive at a mathematical basis of lung surface deformations (lung SDVFs). During the treatment delivery, two ~30–50s of fluoroscopic data (FL) with concurrent VisionRT(VRT) surfaces were acquired pre- and post-treatment. Isometric embedding (Isomap) was used to extract three features from the VRT surfaces. Temporal relation between two data sets was established and the data was partitioned into training and validation datasets. For each FL image in the training dataset, a simulated annealing optimization routine was used to arrive at optimal lung SDVF PC coefficients. These coefficients, along with the corresponding surface features were used to train a motion model that was subsequently validated using the validation dataset.
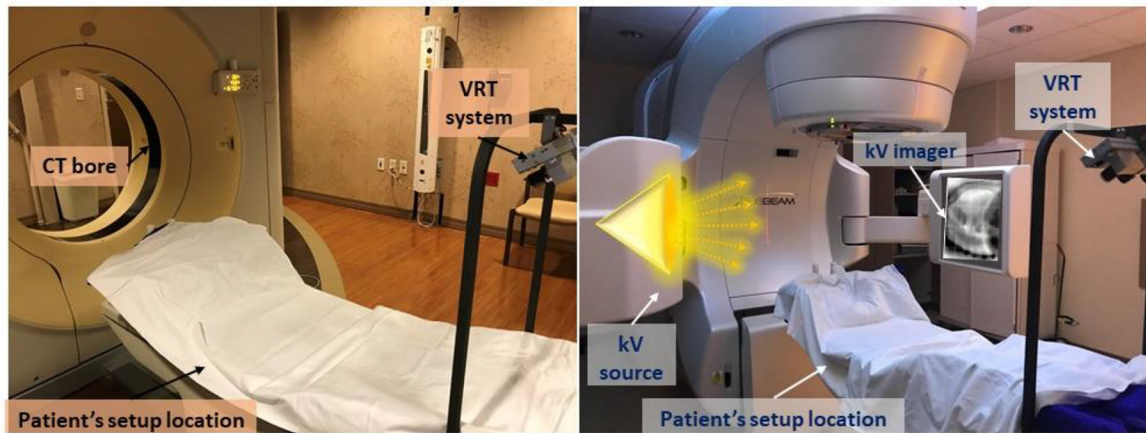
Figure 2- Setup for patient data acquisition during CT simulation and treatment delivery.
A) The couch mounted VisionRT (VRT) system was placed on the CT couch and used
to monitor the thoracoabdominal surface during the CT simulation. **B)** During treatment
delivery, prior to the first beam, and following the last beam, two ~30–50s long fluoroscopic
timeseries with concurrent VRT surfaces were acquired.
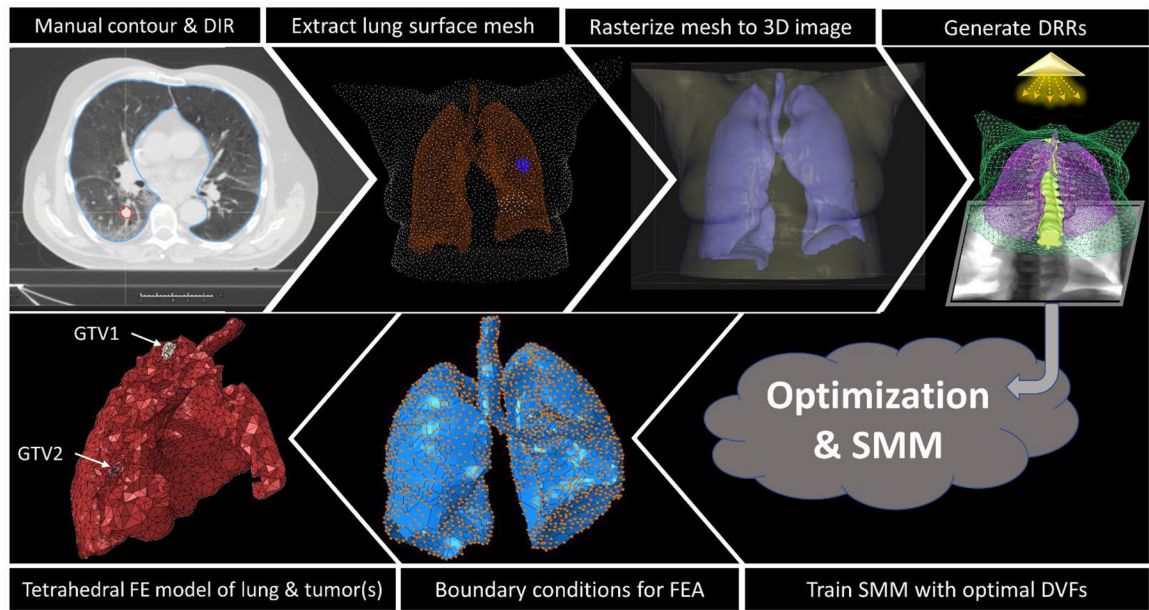
Figure 3- Mesh contouring, extraction and rasterization process for the SMM.
Following contouring and deformable image registration in RayStation TPS, fine triangular
meshes of the body, lung, and vertebrae were exported. Mesh structures were rasterized to a
3D image, and digitally reconstructed radiographs were generated and used as part of model
input. The SMM provides lung surface boundary deformations, which can be used as BCs in
a finite element model of the lung and tumor.
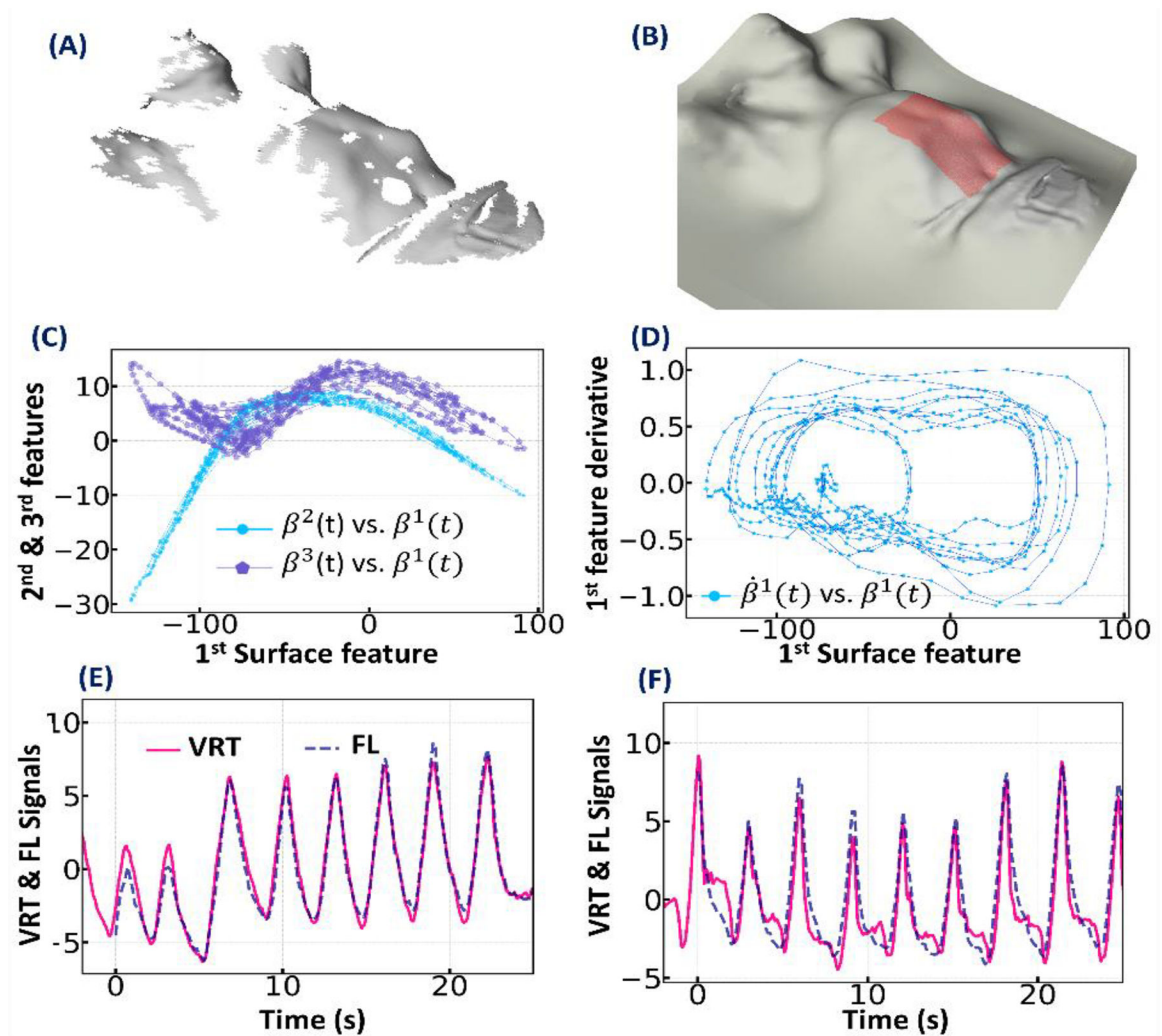
Figure 4- Captured point clouds, reconstructed surfaces, Isomap extracted surface features, and their relations with diaphragm motion.

A) VisionRT point clouds containing points and connectivity. Geometric distortions result in missing patches. **B)** Water-tight surface generated using the Poisson reconstruction algorithm. An ROI patch was used for subsequent analysis. **C)** Relation between the first three surface features extracted via Isometric Embedding. **D)** Relation between the first feature and its time derivative. **E)** Overlap between mean surface displacement, and a patch on the diaphragm tracked from fluoroscopic images for patient 1. **F)** Overlap between mean surface displacement, and patch on the diaphragm tracked from fluoroscopic images for a patient treated with compression belt (patient 5).
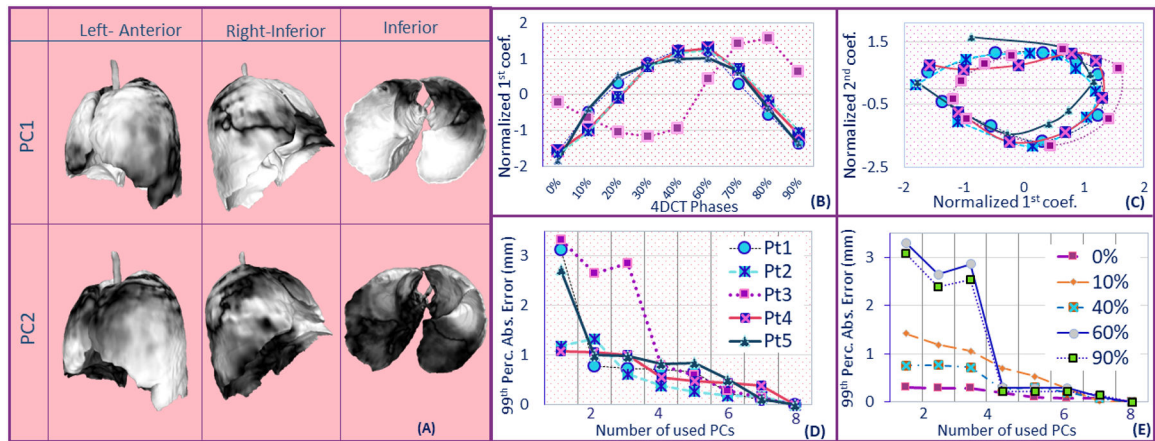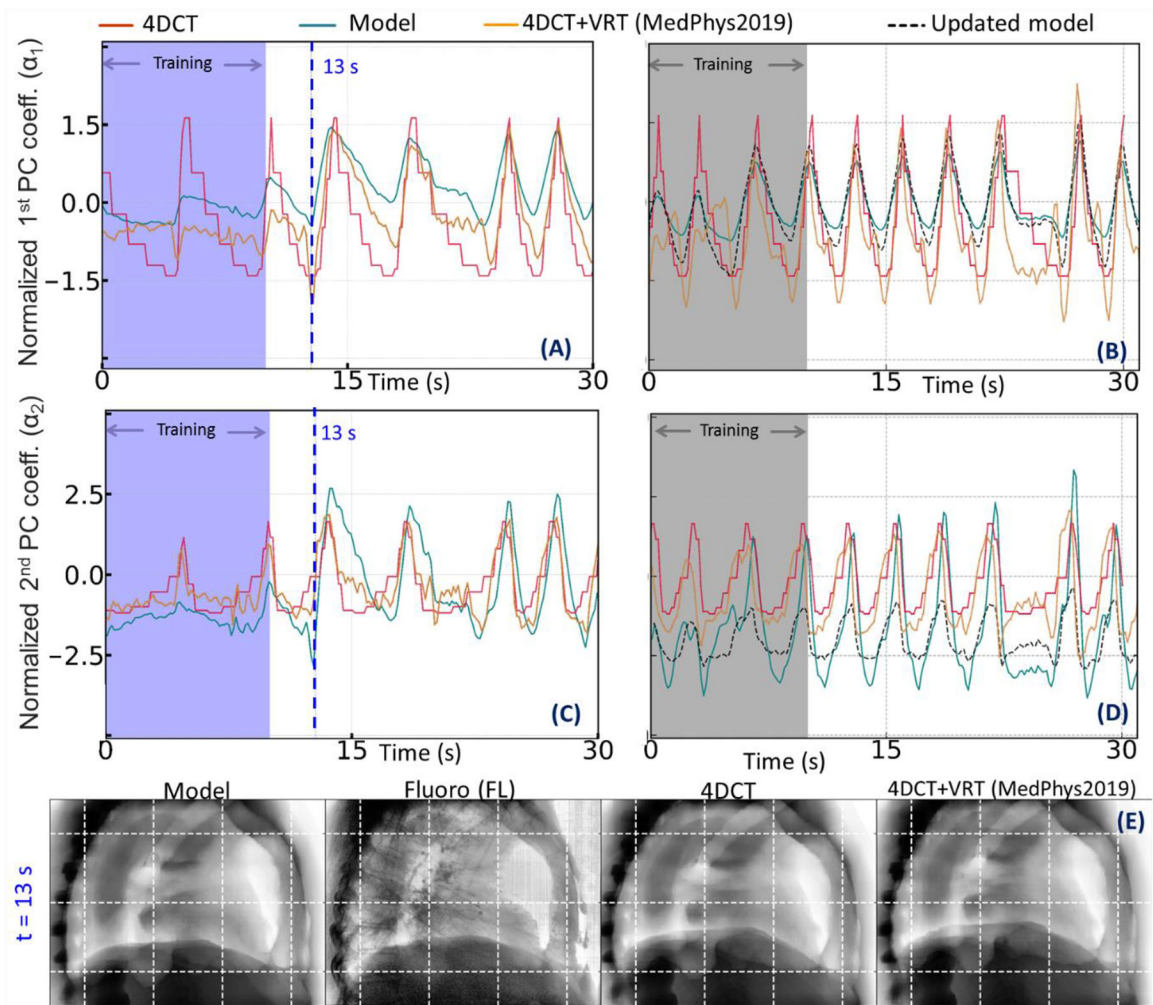
Figure 5-

A) Representation of the first two lung SDVF PC vectors U_1 and U_2: light regions represent regions that exhibited motion. **B)** Variation of normalized 1st coefficient $\alpha^1_{50\% \rightarrow j}$ oefficient with breathing phase for five patients studied in this work. **C)** Variation of the normalized two PC coefficients $\alpha^1_{50\% \rightarrow j}$ and $\alpha^2_{50\% \rightarrow j}$ for all patients. **D)** Convergence of the 99th percentile absolute error (maximum value over all phases) with increasing PC used in equation (1). **E)** Convergence of 99th percentile absolute error with increasing number of PC used in equation (1) for different breathing phases of Patient#3A slower convergence is observed for phases 60% and 90% due to presence of artifacts.
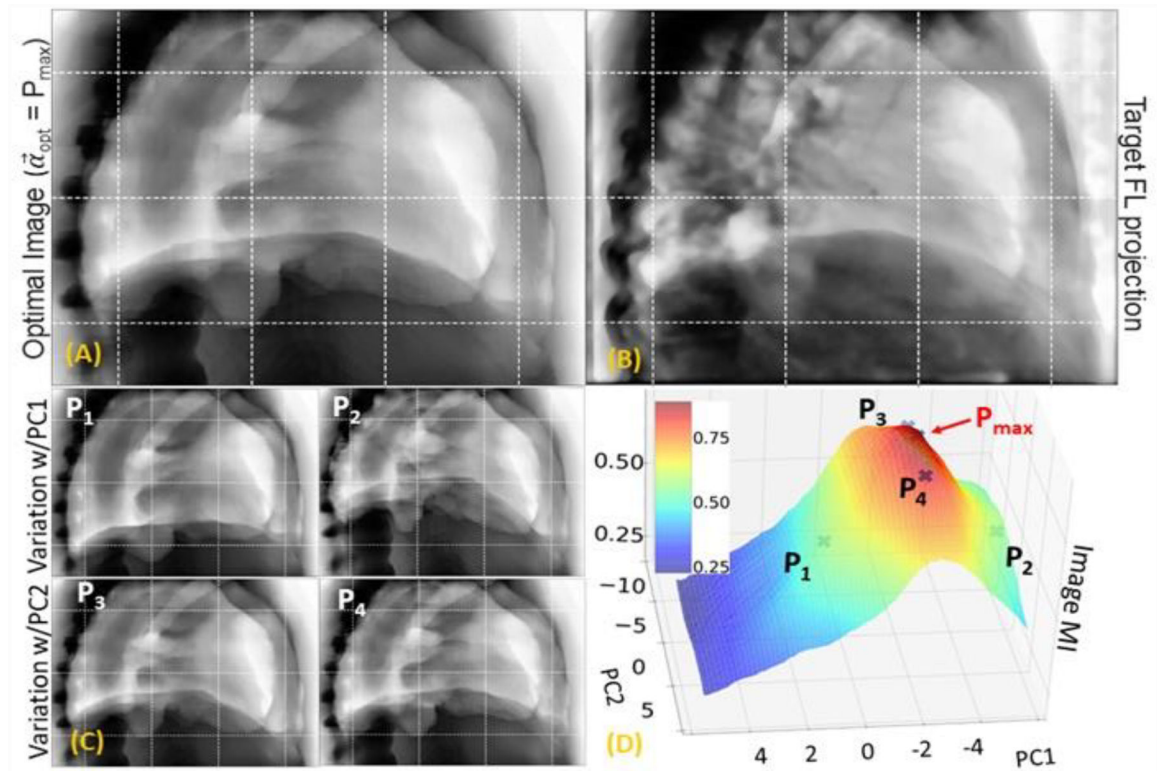
Figure 6- Examples of lung surface deformation vector field optimization process for Patient 1.
A) Optimal right lateral digitally reconstructed radiograph for Patient1 was generated by deforming the lung surface using optimal PC coefficient $\vec{\alpha}_{opt}$. **B)** Right lateral FL frame used as the target image in the optimization procedure. **C)** Impact of the variations in the first two PC coefficients as observed in right lateral radiographs. **D)** Surface of image mutual information (MI) parameterized with first two PC coefficients.
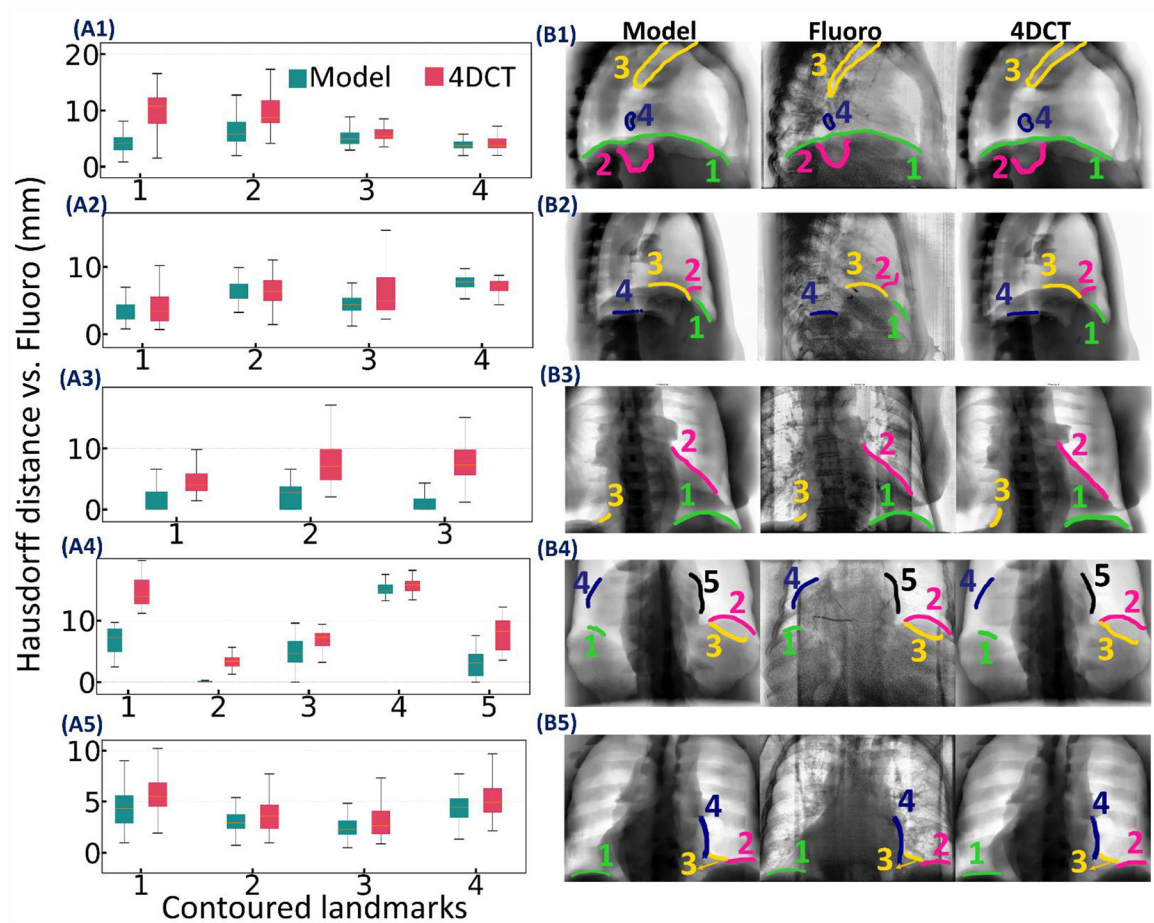
Figure 7-

A) Comparison of phase-assigned 4DCT (red), model (green), and our previous 4DCT+VRT model (yellow) estimated PC1 normalized coefficient α1 for Patient1. B) Effect of model update (dotted black) on the normalized PC1 coefficient for the post-treatment FL acquisition. C) Comparison of model, 4DCT phase-assigned, and our previous 4DCT+VRT model for estimated PC2 coefficient α2 for Patient1 during FX3-start acquisition. D) Effect of model update (dotted black) on the normalized PC2 coefficient. E) Comparison of model, FL image, 4DCT, and 4DCT+VRT images at t=13s of FX3-start.
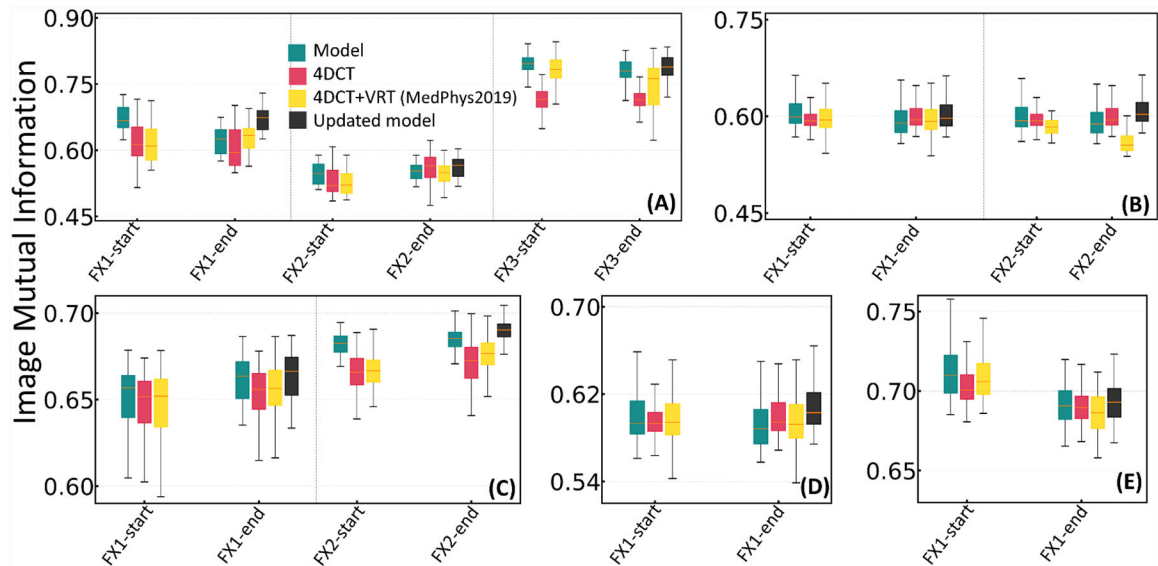
Figure 8- Image Mutual Information score for 9 pairs of FL acquisitions in five lung-SBRT cancer patients, as a function of treatment fraction number and timing around dose delivery. Patients 1–5 correspond to panels A-E. Model constructed using the pre-treatment data is shown in green, updated model using post-treatment data is shown in black, 4DCT is shown in red, and the 4DCT+VRT from our previous work is shown in yellow. (Ranjbar, Sabouri et al. 2019)

Figure 9- Comparison of model and 4DCT performance for landmark position estimation.
In the left column, A1-A5 are the Hausdorff distances from the fluoroscopic reference, for model and 4DCT-estimated landmarks (in mm). On the right, B1-B5 show the landmarks used in the computation for patients 1–5.

Table 1

Lung volumes at end of inspiration (EI) and end of expiration (EE) for the cohort of patients. Each lung surface was discretized as fine triangular meshes using the reported number of nodes (# nodes (N)). (RLL: Right Lower Lobe, RL: Right Lung, LUL: Left Upper Lobe, RUL: Right Upper Lobe).

Patient	Sex	EI (cm³)	EE (cm³)	# nodes (N)	Age	Tumor Size (cm³)	Location	#kV images (duration)	VRT ROI Length×Width (cm²)
1	M	5,090	4,420	139,478	74	2.4	RLL	1679 (240 s)	34×15
2	M	2,790	2,551	95,410	70	2.34	RL	402 (57 s)	28×15
3 *	F	3,755	3,523	119,193	91	10.5	LUL	1425 (203 s)	29×12
4	M	3,142	2,512	101,350	65	0.14,1.81,1.35	LUL,RUL,RLL	370 (53 s)	28×13
5	M	5,107	4,609	143,090	77	9.82	RUL	365 (52 s)	28×12
AVG		3,977	3,523	119,704	75	4	TOTAL	4241 (605s)	31×13

*
4DCT for patient 3 suffered from phase miss-assignment. Maximum and minimum lung volumes are reported as volumes for EI and EE.